Investigation of the Intra-Annual Variability of the North Equatorial Countercurrent/North Brazil Current Eddies and of the Instability Waves of the North Tropical Atlantic Ocean Using Satellite Altimetry and Empirical Mode Decomposition

JEAN-LUC MÉLICE AND SABINE ARNAULT

LOCEAN-IPSL, UMR CNRS/IRD/UPMC/MNHN, Université Pierre et Marie Curie, Paris, France

(Manuscript received 22 February 2017, in final form 14 September 2017)

ABSTRACT

The intra-annual variability of the tropical Atlantic Ocean north of the equator is investigated with satellite altimetry mean sea level anomaly data and with an algorithm based on empirical mode decomposition (EMD) methods. Two regions of high variability are identified. The first region, between 3° and 12°N, is characterized by the presence of westward-propagating eddies linked to the North Brazil Current (NBC) retroflection in the vicinity of the Brazilian coast. They show a strong annual cycle. In this paper the EMD algorithm points out that this signal is frequency modulated shifting from large length-scale structures in October to smaller ones in March. Consequently, the number of ''eddies'' per year can be aliased, according to the time and location of sampling, and can impact the percentage they explain of the interhemispheric exchange of mass and heat associated with the meridional overturning circulation's upper limb. A scenario concerning this dynamics is proposed. The second region reveals the presence of westward-propagating instability waves centered north of the equator (3°–7°N) between 50° and 10°W. These instability waves are also frequency modulated and show a strong seasonal cycle with maximum amplitude around August.

1. Introduction

The tropical North Atlantic, between 3° and 12°N, is characterized by the presence of westward-propagating eddies linked to the North Brazil Current (NBC)/North Equatorial Countercurrent (NECC) retroflection. The rings are shed in the vicinity of the Brazilian coast where the NBC forms a strong meander that retroflects into the NECC. After separating from the retroflection region, the rings travel northwestward along the Brazilian coast. Since their first description a decade ago (Johns et al. 1990; Didden and Schott 1993; Richardson et al. 1994; Fratantoni et al. 1995), these structures have received increasing attention, as they may constitute an important component of the upper limb return flow of the meridional overturning circulation (MOC) by contributing to the northward transport of southern Atlantic water into the northern subtropical gyre (e.g., Pauluhn and Chao 1999; Goni and Johns 2001; Fratantoni and Glickson 2002; Goni and Johns 2003; Johns et al. 2003; Fratantoni and Richardson 2006; Jochumsen et al. 2010). Other mechanisms include possible shallow coastal currents along the South American shelf and Ekman transport in the ocean interior (Candela et al. 1992; Mayer and Weisberg 1993; Fratantoni et al. 2000; Halliwell et al. 2003). Previous studies stated that these rings may account for 25% of the interhemispheric exchange of mass and heat associated with the meridional overturning circulation's upper limb (Johns et al. 1990; Didden and Schott 1993; Richardson et al. 1994; Fratantoni et al. 1995). Goni and Johns (2001) increase this percentage to more than 30%, while Garzoli et al. (2003) contend that these rings may be responsible for more than 50% of the interhemispheric exchange. These different percentages are explained by the different estimates of the number of rings and their characteristics made by these authors. Table 1 summarizes the characteristics of the eddy structures issued from these studies. The number of eddies per year varies from 2 to 9. The propagation velocities range between 8 and 18 cm s^{-1}. The ring length scales extend from 195 to 400 km. Thus, their relevance for the northward transport of South Atlantic water clearly depends on their frequency of generation as well as on their horizontal and vertical structures. Fratantoni et al. (1995), from both observations and modeling, were one of the few authors to notice a seasonal modulation in these characteristics. For instance, they found a ring diameter varying from 70–100 km in March to

Corresponding author: J. L. Mélice, jlmelice@locean-ipsl.upmc.fr

DOI: 10.1175/JTECH-D-17-0032.1

TABLE 1. Mean characteristics of the eddies and mesoscale structures as noted in previous studies.

Investigator	Rings per year (w.r.t. years in other studies)	Ring length scale (km)	Propagation velocity (km day^{-1})
Johns et al. (1990)	3–4 (1987–88)	400	10–15
Didden and Schott (1993)	2 (Nov 1988–Jun 1989)	250	13
Richardson et al. (1994)	3–4 (1989–92)	250	8–12
Fratantoni et al. (1995)	3–5 (Sep 1987–Aug 1998 for the data)	250 (Nov–Mar) 70–100 (Mar–Jun)	8–16
Pauluhn and Chao (1999)	3–4 (Dec 1992–Jun 1997)	200–600	14
Goni and Johns (2001)	2–6 (Oct 1992–Dec 1998)	195	14
Frantantoni and Glickson (2002)	5 (Sep 1997–Sep 2000)	200–300	12.5
Johns et al. (2003)	8–9	200–320	
Garzoli et al. (2003)	6–7 (Nov 1998–Jun 2000)	392	12.4
Goni and Johns (2003)	3–7 (Nov 1992–Dec 2001)	200	
Fratantoni and Richardson (2006)	3	200–300	13
Jochumsen et al. (2010)	6–7 (model)	360 (250 Lesser Antilles)	
Castelão and Johns (2011)	7 (Nov 1998–Jun 2000 for the moorings)	85–158	

250 km in November. But they did not give any information for these differences. Athié and Marin (2008) also identified a frequency difference in their structures along 5°N east and west of 30°W but again without any explanation. From a geophysical dynamics point of view, Nof and Pichevin (1996) explain this western variability by purely local instability processes or momentum balance. Other authors involve a remotely propagating influence originating in the interior (Johns et al. 1990; McClean and Klinck 1995). According to Jochum and Malanotte-Rizzoli (2003), the mechanisms governing their generation, detachment, and propagation pose a very interesting and complicated dynamical problem. The interaction between eddies and tropical instability waves (TIWs), for instance, has been discussed.

TIWs are known, since the pioneer works of Düing et al. (1975), Weisberg (1980), Legeckis (1977), and Philander et al. (1986), for instance, to be a common large-scale propagating feature of the tropical ocean variability. TIWs play a role in climate variability, as they can influence the phase of the seasonal cycle, and the position of the equatorial cold tongue and of the intertropical convergence zone (ITCZ), the oxygen, and salinity front along the equator, and the plankton and nutrient distribution (Menkes et al. 2002 ; Jochum and Malanotte-Rizzoli 2003; Lee et al. 2012). Different types of TIWs can exist, depending on the region: Yanai waves at about 17 days, characterized by fluctuations in meridional velocity at the equator and in subsurface temperature at 2°N and 2°S; and unstable Rossby waves at about 33 days, characterized by the subsurface temperature at 5°N (Lyman et al. 2007; Bunge et al. 2007; Han et al. 2008; Lee et al. 2012; Yin et al. 2014). Theoretical studies (e.g., Philander 1978; Jochum et al. 2004) have related the phenomenon to the instability of the strong zonal flows that characterize the circulation in all three equatorial oceans although other factors, such as Kelvin–Helmholtz instability, could occur (Proehl 1996). It is usually assumed that TIWs are predominantly generated by barotropic instabilities as a result of the meridional shear between the northern South Equatorial Current (nSEC) and the NECC or the shear between the nSEC and the Equatorial Undercurrent (EUC), and that the baroclinic instabilities related to the vertical shear of the mean current are negligible (Weisberg and Weingartner 1988; Philander et al. 1986; Kelly et al. 1995; Jochum et al. 2004). However, McCreary and Yu (1992), using a nonlinear 2.5-layer model, find that their surface-trapped instability is primarily frontal (baroclinic) instability. Grodsky et al. (2005) suggest, from in situ data at 23°W, that both processes are important, as do von Schuckmann et al. (2008). These authors find that in the Southern Hemisphere, TIWs are forced only by baroclinic instabilities associated with the vertical shear of the SEC. In the Northern Hemisphere, baroclinic instability caused by the vertical shear of the nSEC and barotropic instabilities caused by horizontal shears of the EUC/nSEC and nSEC/NECC contribute. Some questions are still pending about their occurrence, their location, and the way they could interact with other phenomena.

Valuable global datasets such as altimetry datasets have become precious allies for oceanic investigations from long and basinwide time series. With nearly 30 years of data, satellite altimetry now offers a unique opportunity to explore this variability in detail, in particular propagating structures, which are an important component of the tropical ocean variability. A critical point now is to establish methods to identify the processes through these data, to point out their potential modulation in time, and to establish their connection. To our knowledge, the empirical mode decomposition (EMD) method is one of the few methods answering these criteria. The

EMD has been recently used in oceanography studies. For instance, the EMD was applied by Salisbury and Wimbush (2002) to predict future El Niño events from the Southern Oscillation index. Autret et al. (2013) detect, from sea surface temperature (SST) data around Antarctica and EMD, an 8-yr rotating wave that could be linked to the Antarctic circumpolar wave. Sea level variations have also benefited from this method (Breaker and Ruzmaikin 2011; Ezer and Corlett 2012; Ezer et al. 2013; Lee 2013; Chen et al. 2014), although Chambers (2015) suggest that using EMD to identify multidecadal variability and accelerations in sea level records should be used with caution. In this paper, we have developed an algorithm that is based on the EMD method. This algorithm is very efficient for separating automatically (without any a priori cutoff period) the amplitude- and frequency-modulated high- and low-frequency components of the signals. Here, we apply our EMD-based algorithm to altimetric data in the tropical North Atlantic Ocean in order to improve our knowledge of wave and propagating feature dynamics. The purpose of this paper will be therefore to determinate with more precision the intra-annual characteristics of the northwestern Atlantic tropical eddies (as, for instance, the number of eddies per year and per season) and the TIW, as well as their time-varying lengths, modulations, interactions, and spatial distributions.

The paper is organized as follows: In section 2 we describe the altimetry [sea level anomalies (SLA)] data and the mathematical methods used. We focus on the intra-annual variability, and thus on the anomalies of the SLA signals in the tropical North Atlantic. In section 3, we first investigate the SLA with the empirical orthogonal functions (EOFs). In section 4 we describe the frequency characteristics of these anomalies between 3° and 12°N, and in section 5 we investigate the characteristics of the eddies linked to the NECC/NBC and the instability waves in the same domain with the complex orthogonal functions (C-EOFs). The discussions and conclusions are presented in sections 6 and 7, respectively.

2. Data and methods

The altimetry data used in this study were downloaded from the AVISO data center (http://www.aviso.oceanobs.com). They consist of SSALTO/DUACS SLA merged products. The data from all altimeter missions (*Jason-1* and *Jason-2*, TOPEX/Poseidon, *Environmental Satellite* (*Envisat*), *Geosat Follow-On*, *ERS-1* and *ERS-2*, and *Geosat*) are processed by the SSALTO/DUACS system in order to provide a consistent and homogeneous catalog of products for varied applications, both for near-real-time applications and offline studies (see http://www.aviso.oceanobs.com/fr/donnees/informations-sur-les-produits/duacs/index.html for more information). We use the new multimission altimeter dataset reprocessing DUACS DT2014 (Pujol et al. 2016), whose main priority was to improve the monitoring of the mesoscales in the global ocean. The series extends from January 1993 to September 2015. We use the "two satellite" series in order to keep interannual homogeneity. Our domain is 20°N–20°S, 60°W–20°E with a grid resolution of 1/4° × 1/4°. As we focus on the intra-annual variability, the analyses will be performed on the anomalies of the SLA signals. By taking the anomalies, the seasonal signal, which is known to be dominant in the tropical Atlantic Ocean (e.g., Merle et al. 1980; Arnault and Cheney 1994), is therefore filtered. All periods above one year are also eliminated with a Butterworth filter.

The mathematical methods used in this study are the already mentioned EOF, C-EOF, EMD, and Hilbert transform (HT). The novelty of this study is to adapt the EMD method to oceanic satellite data. We will show in the next sections that the different processes investigated here can be analyzed with precision if the SLA signals at each grid point are decomposed into their high-frequency (HF) and low-frequency (LF) components. Emphasis will be put on the real and imaginary parts, amplitude (modulus or envelope), and phase (frequency) of the HF and LF components. These characteristics are obtained via the HT (Poularikas 1996; Cohen et al. 1999).

These HT-obtained characteristics are mathematically valid and interpretable in a way that is meaningful and representative of physical phenomena only if the HF and LF components are asymptotic (e.g., Delprat et al. 1992; Vakman 1996; Picinbono 1997; Cohen et al. 1999). By definition, an asymptotic signal is monocomponent. A monocomponent signal is described in the time–frequency plane by a single ridge and is therefore characterized by one unique frequency at any time t. The set of monocomponent signals includes, for instance, single sinusoids but also signals like chirps, which can be amplitude modulated. The algorithm developed for the extraction of the asymptotic HF and LF components of the signals is based on the EMD (Huang et al. 1998; Rilling et al. 2003, 2007).

a. *Empirical mode decomposition (Hilbert–Huang transform)*

The fundamental part of the Hilbert–Huang transform is the EMD. Using the EMD method, any complicated dataset can be decomposed into a finite and often small number of components, which is a collection of intrinsic mode functions (IMF). An IMF represents a generally simple oscillatory mode. By definition, an IMF is any

function with the same number of extrema and zero crossings, with its envelopes being symmetric with respect to zero. The definition of an IMF guarantees a well-behaved HT of the IMF. Therefore, the IMF is an asymptotic signal and we can extract its real and imaginary parts, amplitude (modulus or envelope), and frequency.

The EMD decomposes the signal into IMFs by a shifting process as follows:

1) For the signal $x(t)$, let m_1 be the mean of its upper and lower envelopes as determined from a cubic-spline interpolation of local maxima and minima.
2) The first component h_1 is computed: $h_1 = x(t) - m_1$.
3) In the second sifting process, h_1 is treated as the data and m_{11} is the mean of h_1 upper and lower envelopes: $h_{11} = h_1 - m_{11}$.
4) This sifting procedure is repeated k times, until h_{1k} is an IMF, that is, $h_{1(k-1)} - m_{1k} = h_{1k}$.
5) The operation ends when the residue contains no more than one extremum.
6) The original signal $x(t)$ can be reconstructed by summing the different IMFs.

b. *HF and LF decomposition based on the EMD method*

The algorithm is as follows:

1) We take a cutoff period p increasing by a step of one week from 3 and 51 weeks (i.e., p = 3, 4,..., 50, 51 weeks).
2) For all of these values of p, the HF component (periods from 2 to p weeks) and the LF component (periods from p to 52 weeks) are extracted with a Butterworth filter.
3) The first IMF of the EMD for each HF and LF component (HF IMF-1 and LF IMF-1, respectively) is then computed. We note that only the first IMF of the EMD is used and that with our data this first IMF always explains the highest percentage of variance of all the IMFs of the EMD.
4) The p (and therefore the HF and LF IMF-1s), which is finally selected, is the one for which the sum of the two IMF-1s explains the maximum percentage of the variance of the original signal.

The p varies at each grid point from ~6 to ~12 weeks over the basin (Fig. 1a). Averaging these cutoff periods between 3° and 12°N gives a mean value of 8.3 weeks. Figure 1b gives the percentage of the variance at each grid point of the raw signal anomalies, which is explained by the sum of HF IMF-1 and LF IMF-1. It is usually over 70%. Between 3° and 12°N, this percentage of the variance varies from 74% to 95% (mean = 84%). The definition of an IMF guarantees that the HF IMF-1 and LF IMF-1 components are asymptotic. In the next sections, HF and LF will refer to HF IMF-1 and LF IMF-1, respectively.

3. EOFs of the SLA

The standard deviation (std dev) of the SLA is displayed in Fig. 2 and the ridge of maximum std dev (white line) is superimposed. The largest part of the variability is located between 5° and 15°N near the South American coast. The standard deviation values reach more than 7 cm in that area, whereas most of the basin stays within 3 cm. This maximum extends north of the usual annual amplitude extremum, described, for instance, by Arnault et al. (1989) and Carton (1989) during the first altimetric analyses of the tropical Atlantic Ocean from *Geosat*, and is associated with the ITCZ migration.

An EOF analysis is performed on the SLA restricted to the ridge of maximum std dev displayed in Fig. 2, either for its western part (60°–43°W) or for its eastern part (30°–10°W). The homogeneous correlation maps [i.e., the correlation between the principal component (PC) and the anomalies at each grid point] of the PC-1 West and PC-2 West (Figs. 3a,b, respectively) show some kind of ''eddy'' structures along the northern coast of America between 0° and 10°N in the region where the standard deviation is the highest. From the PC information, the results show that these structures have a period of ~7 weeks. Propagation of structures is indicated by two successive EOFs explaining a similar amount of variance and whose patterns are in quadrature. This is typical here of EOF-1 and EOF-2. Moreover, there is a shift in time (not shown) corresponding to a quarter of a wavelength between the PCs. We suggest that these ''eddies'' are instabilities generated by the retroflection of the NBC to the NECC in the vicinity of the Brazilian coast. The homogeneous maps of PC-1 East and PC-2 East (Figs. 3c,d) show the presence of two different processes at the same latitude, which could be linked to Rossby (and Kelvin equatorward) waves for PC-1 East with a period of about 13 weeks and instability waves for PC-2 East with a period of about 5 weeks.

4. Frequency characteristics of the SLA on the ridge between 3° and 12°N

The SLA on the ridge of maximum variance (Fig. 2) are also analyzed in the frequency domain with the continuous wavelet transform (CWT) to refine their spatial high-/low-frequency distribution. The global CWT spectra, calculated at each grid point of the ridge, are displayed in Fig. 4a. They confirm the presence of high- and low-frequency components along the ridge except in

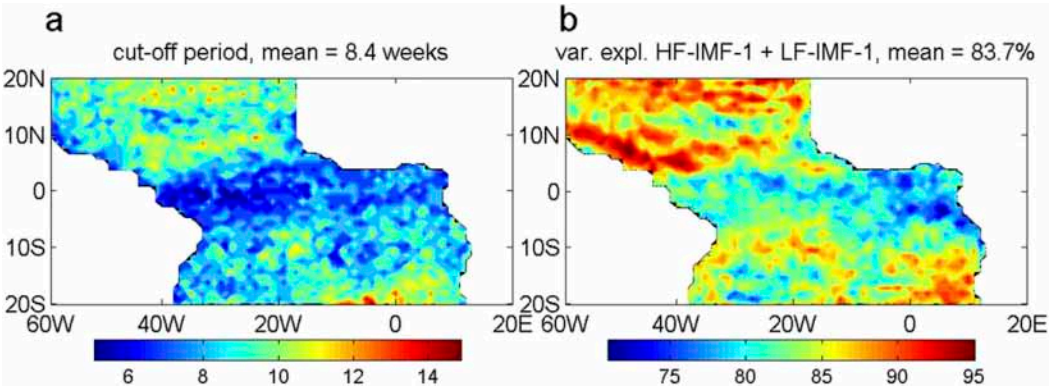

FIG. 1. (a) Cutoff period obtained from the EMD algorithm over the tropical Atlantic Ocean (weeks). (b) Percentage of variance (compared to the raw mapped SLA signal) explained by the sum of the HF IMF-1 and the LF IMF-1 components of the EMD decomposition.

the center of the basin, where only LFs seem to be present. The western part of the ridge is also, as expected, far more energetic than the eastern one. We decomposed the anomaly signals in their HF and LF components via the algorithm based on the EMD technique described in section 2. Their corresponding main periods are displayed in Fig. 4b. They remain rather stable along the ridge around 5–7 weeks for the HF components and vary around 10–16 weeks for the LF components. The standard deviations of these HF/LF components are shown in Fig. 4c. The percentage of variance of the sum of the HF and LF components explained by the HF and LF components are displayed in Fig. 4d. As suggested by the previous figures, the signals near the Brazilian coast around 59°W are mainly composed of energetic HF components, while those in the central basin near 41°W are mainly composed of LF components. The signals, linked to the instability waves, around 17°W are mainly composed of HF components, while the signals, linked to the Rossby waves, around 10°–30°W are characterized by LF components. However, both of these are far less energetic than their western counterparts. Two node points (when LF and HF signals are equivalent in the explained percentage of variance) exist at 48° and 27°W.

We also look at the frequency and amplitude modulations of the components, and more precisely how the HF and LF components are distributed in time. We analyze, for instance in Fig. 5, the SLA signal on the ridge at 48°W, where each component explains the same part of the variance (Fig. 4d). Their sum explains 81.3% of the SLA (Fig. 5a). The HF and LF components and their envelopes (modulus or amplitude modulation) are displayed in Figs. 5b,c, respectively. The superimposition of these components on the signal is given in Figs. 5d,e. As noted previously, these envelopes allow us to see how the HF and LF components are distributed in time. The striking feature in this distribution is the presence of a strong seasonal cycle: the signal is mainly composed of HF components around February–March and is mainly composed of LF components around October. The same computations at 27°W, the other node in Fig. 4d, present HF components peaking in August, with secondary activity but less energetic by the end of the year. There is also a seasonal cycle in the LF component; however, it is more vague, although some indication of an activity peaking in boreal fall can be suggested (not shown).

5. Characteristics of the eddies linked to the NECC and the instability waves

To enhance the dynamical modes that are involved in the northwestern part of the tropical Atlantic basin, we use the C-EOF technique [see Navarra and Simoncini (2010) for a description of the method]. The C-EOF allows us to estimate the speed of the propagating modes and some other characteristics, such as their amplitude

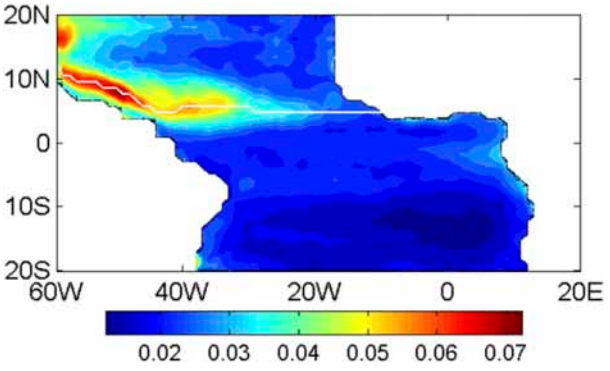

FIG. 2. Std dev (m) of the SLA and maximum std dev ridge (white line).

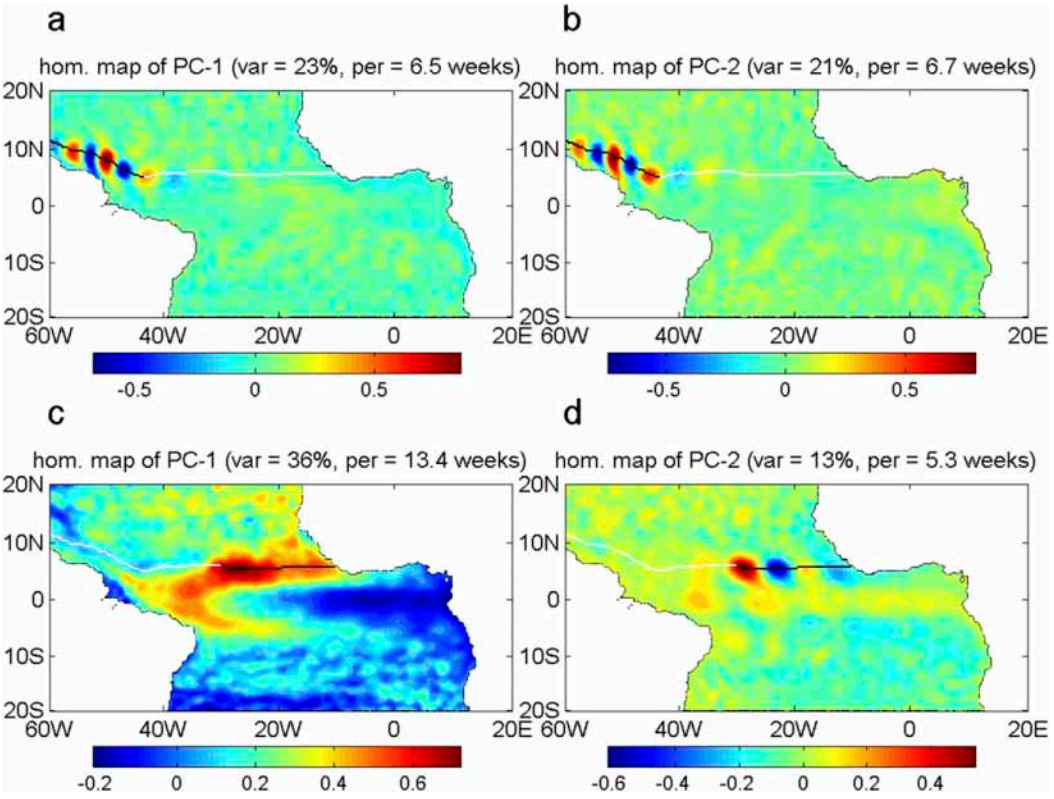

FIG. 3. (a) Homogeneous correlation map of the PC of the EOF-1 of the SLA restricted on the ridge of Fig. 2 from 60° to 43°W (black line). (b) As in (a), but for EOF-2. (c),(d) As in (a),(b), but from 30° to 10°W.

and frequency modulations, but it can be applied only if the signals are asymptotic. Therefore, the analysis will be performed on the HF and LF asymptotic components of the signals.

We focus our study on the NECC and the instability wave region between 3° and 12°N. The first C-EOF of the HF and LF components are displayed in Figs. 6a,b. The patterns of the real and imaginary parts are in quadrature. They show a structure of westward-propagating eddies close to the Brazilian coast. The HF structures are limited to the west of 45°W, whereas the LF structures extend from 30° to 55°W. However, the LF components present larger eddies around 42°W and smaller ones around 59°W. The length scales seem also smaller for the HF structures than for the LF structures: the diameters of the eddies are ~2.5° at 59°W longitude for the HF components and ~5° at 42°W for the LF components. The second C-EOF of the HF and LF components (not shown) displays the same patterns as the first C-EOF. The third C-EOF of the HF component (Fig. 6c) shows the presence of westward-propagating structures from 10° to 35°W and along 5°N. The length scale is ~10° of longitude. Their location and length scales are typical to those observed in TIWs and their PCs present a maximum in boreal summer. This point will be discussed later.

The speed of the propagation of these structures is estimated from the characteristics of the C-EOFs, and from the main period of their PCs, which are 5.8, 15.9, and 5.2 weeks for the HF C-EOF-1 (Fig. 6a), the LF C-EOF-1 (Fig. 6b), and the HF C-EOF-3 (Fig. 6c), respectively. The mean speed obtained is 14 km day^{-1} (17 cm s^{-1}) for the coastal eddies (Fig. 6a), 6–10 km day^{-1} (7–11 cm s^{-1}) for the LF "rings" in Fig. 6b, and 29–35 km day^{-1} (34–41 cm s^{-1}) for the "instability waves" (Fig. 6c).

As the HF and LF components are asymptotic, the PCs of the C-EOFs are also asymptotic and their envelopes can be computed. They are displayed in Figs. 7a–c, respectively. They are all characterized by a strong annual cycle. The envelope of PC-1 of the HF component (Fig. 7a) is maximum in March, while the envelope of PC-1 of the LF component (Fig. 7b) is maximum in October, in agreement with the results obtained in Fig. 5. As demonstrated in section 4, this shows that the signals of the NBC/NECC rings are frequency modulated: they are composed of oscillations shifting from HF in March to LF in October [centered on 23 March and 12 October, respectively, according to the sinus wave (red) fitted to the envelope in Figs. 7a,b]. If we consider all values above 0.8 standard deviation (σ),

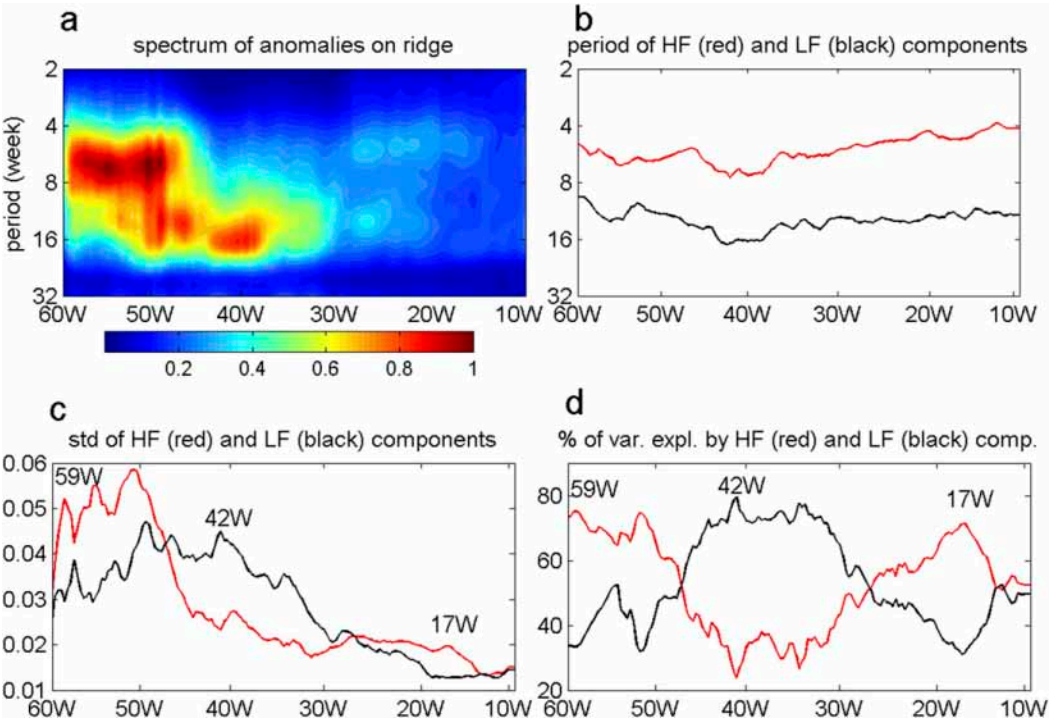

FIG. 4. Frequency characteristics of the SLA on the ridge of Fig. 2. (a) Global CWT spectra of the anomalies, (b) period, and (c) std dev of the HF IMF-1 (red) and LF IMF-1 (black) components. (d) Percentage of variance of the sum of the HF and LF IMF-1 components explained by the HF IMF-1 (red) and LF IMF-1 (black) components.

then the mean number of rings is five per year for PC-1 of the HF component and three per year for PC-1 of the LF component. This will be discussed with more detail in section 6. The instability waves also show a strong seasonal cycle with maximum amplitude in August and a mean period of 5.2 weeks (Fig. 7c).

6. Discussion

In this paper we have applied a relatively new (for oceanographic use) mathematical concept (the EMD) and checked its ability to explore the intra-annual variability of the tropical Atlantic Ocean with satellite altimetry SLA data. With the help of this algorithm, we have found different areas of propagating features.

a. Western NBC/NECC region and rings

The first area occurs in the western NBC/NECC region and along the Brazilian coast (Figs. 6a,b). The decomposition reveals that HF structures are located west of 45°W. They have a diameter of ~250 km and a mean propagation speed of 17 cm s^{-1} (14 km day^{-1}). The LF structures appear between 30° and 55°W with a larger length scale of ~800 km (from ~700 to ~1000 km eastward). Their mean propagation speed is 9 cm s^{-1} (8 km day^{-1}). Both present a strong seasonal cycle with maximum activity in March for the HF component and in October for the LF component.

As mentioned in the introduction, the NBC rings have been extensively studied because of their potential role in interhemispheric transports (Johns et al. 1990; Didden and Schott 1993; Richardson et al. 1994; Fratantoni et al. 1995; Pauluhn and Chao 1999; Goni and Johns 2001; Fratantoni and Glickson 2002; Goni and Johns 2003; Johns et al. 2003; Garzoli et al. 2003; Fratantoni and Richardson 2006; Jochumsen et al. 2010). The results concerning the ring characteristics are highly variable both in length scale or appearance—for instance (Table 1), even when considering the different observation sources (in situ, satellites, models)—and periods. Our results fit into the range of these values, which is large.

The use of a gridded altimetry product instead of the raw alongtrack data in our study can be questionable, as it could influence the scales of the structures. Using alongtrack data means that only one satellite at a time can be used without facing the problems of different characteristics, biases, and corrections between the missions even for missions such as TOPEX/Poseidon/*Jason-1*/*Jason-2*/*Jason-3*, which are very similar regarding their repetitiveness (9.91 days) and the ground

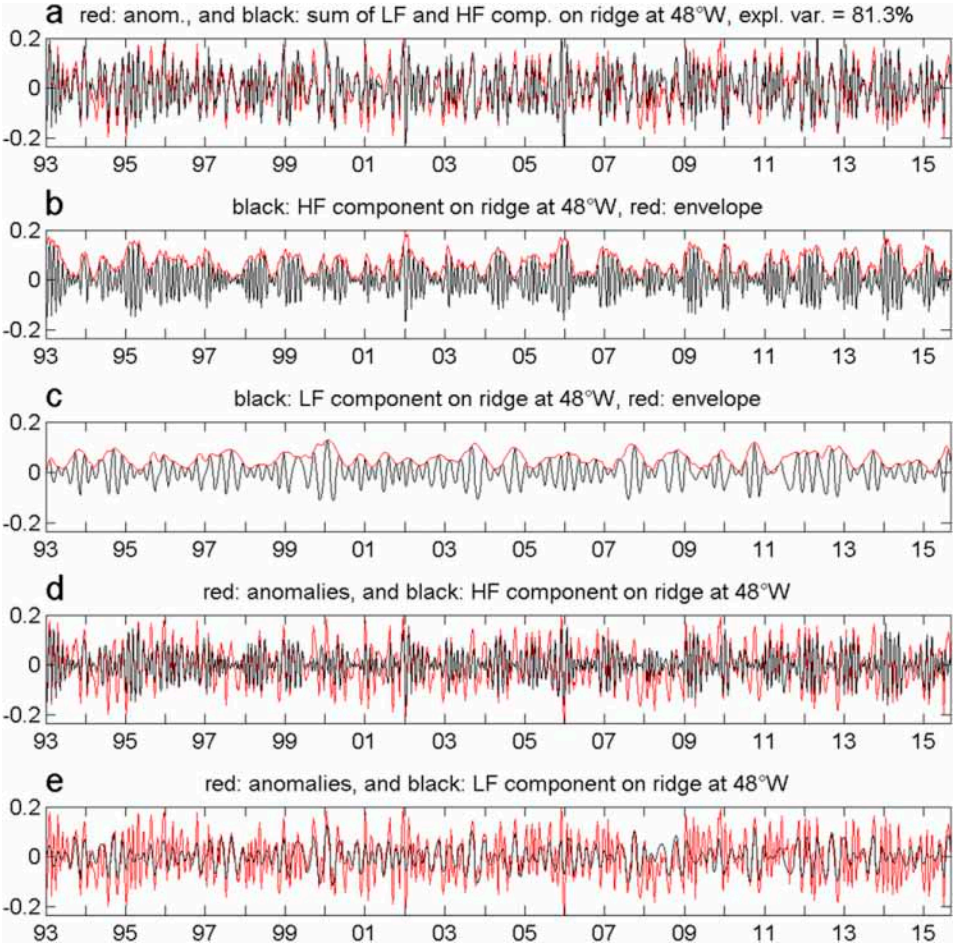

FIG. 5. (a) SLA on the ridge of Fig. 2 at 48°W (red), and sum of the HF IMF-1 and LF IMF-1 components (black). (b) HF IMF-1 component (black) and its envelope (red). (c) As in (b), but for the LF IMF-1 component. (d) SLA on the ridge at 48°W (red) and HF IMF-1 component (black). (e) As in (d), but for the LF IMF-1 component.

track separation at the equator (315 km). The gridded products not only consider the abovementioned missions but missions such as the U.S. *Geosat* and the European *ERS-1* and *Envisat-2*/*Envisat* with other characteristics (17 days and 150 km; 35 days and 80 km, respectively). This merging follows the conclusions of the ''altimetry'' community that at least two altimetry satellites are required to map the ocean and monitor its movements precisely at scales of 100–300 km (mesoscale). The main priority of the new multimission altimeter dataset reprocessing DUACS DT2014 was to improve the monitoring of the mesoscales in the global ocean. It benefitted from climate standards and corrections that do not degrade the mesoscale signals. The parameters used for the mapping procedure—a compromise between the characteristics of the physical field focused on and the altimeter constellation sampling capabilities—were refined, especially the use of better defined correlation scales of the signal to map. For instance, the covariance function used in the optimal interpolation (OI) were shortened and varied both latitudinally and longitudinally, and a more precise estimation of the errors budget associated with the different altimeter measurements was considered. Pujol et al. (2016) mentioned that the DT2014 products—compared to the previous version, DT2010—present additional signal for wavelengths lower than ~250 km, inducing SLA variance and a mean eddy kinetic energy (EKE) increase of +5.1% and +15%, respectively. Figure 8 gives a comparison between the SLA obtained from the OI for 27 March 2014 and two *Jason-2* tracks crossing the area around that date. There is a clear agreement in the scaling of the eddy structures shown by both the OI and the alongtrack data. Thus, the characteristic length scales for the structures revealed by our analysis are not strongly aliased by the OI.

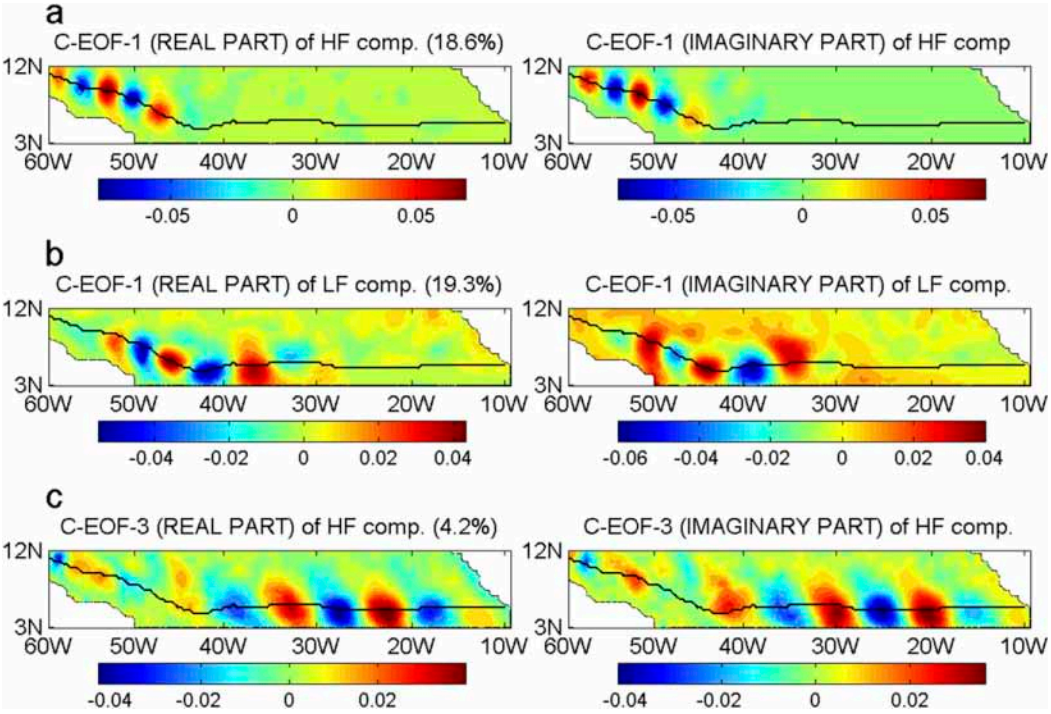

FIG. 6. (a) Real and imaginary parts of the first C-EOF of the SLA HF IMF-1 components between 3° and 12°N. The ridge of Fig. 2 is superimposed (black line). (b) As in (a), but for the LF IMF-1 components. (c) As in (a), but for the third C-EOF of the HF IMF-1 components.

We found a difference in terms of structures: HF lies west of 45°W with a diameter ~250 km, preponderant in March, and LF structures between 30° and 55°W with a larger diameter of ~500 km, and a dominant period in October. Nof and Pichevin (1996) explain this western variability by purely local instability processes or momentum balance. Other authors involve remotely propagating influences originating in the interior (Johns et al. 1990; McClean and Klinck 1995). Our results emphasize these latter scenarios, in particular the sequence enounced

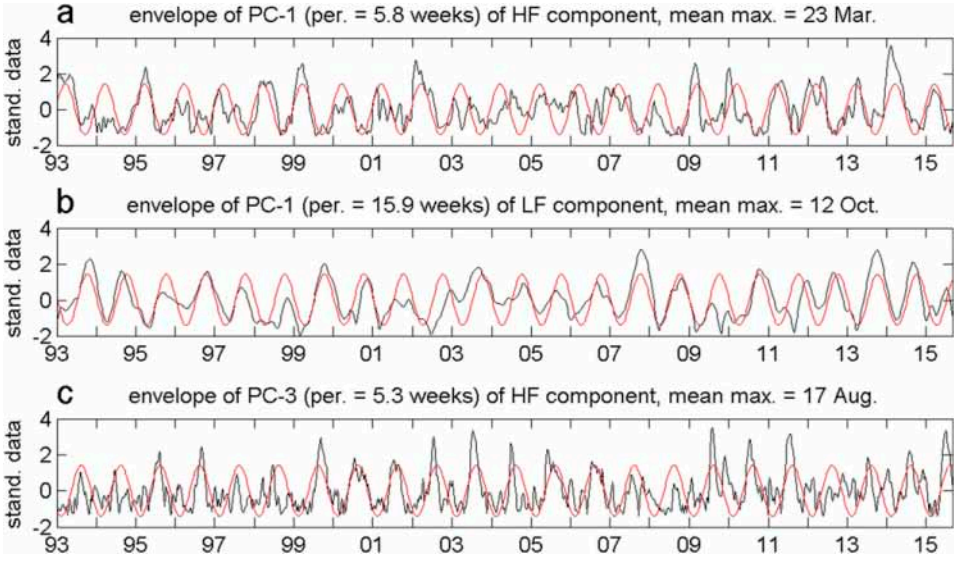

FIG. 7. (a)–(c) Envelopes (black) of the PCs of the C-EOFs in Fig. 6, and fitted sine wave with a 1-yr period (red).

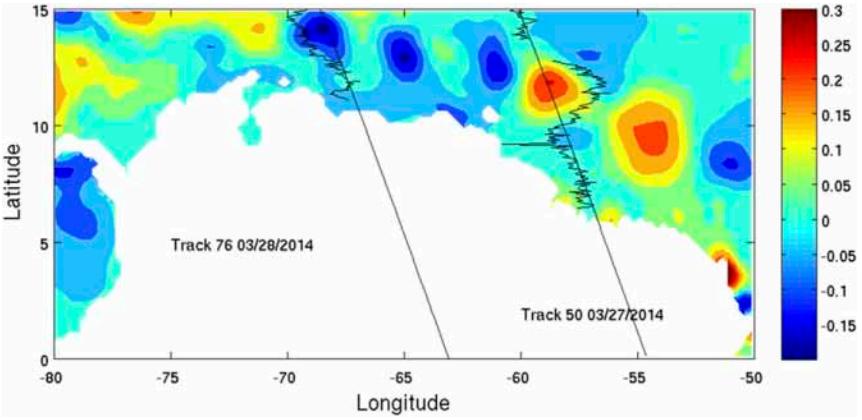

FIG. 8. Result of the AVISO OI on 27 Mar 2014 (shading). Superimposed (black curves) are the alongtrack Geophysical Data Record SLA signals for track number 50 (same day) and track number 76 (the day after).

by Jochum and Malanotte-Rizzoli (2003) from a numerical study: when retroflecting in boreal fall, the NBC produces Rossby waves with a phase speed between ~9 and 13 cm s^{-1}, a meridional wavelength of ~1200 km, and a zonal wavelength between 700 and 900 km. Our computations for these structures present a phase speed of ~9 cm s^{-1}, a meridional wavelength of ~1050 km, and a zonal wavelength between 700 and 1000 km. The wavelength and phase speed of the first baroclinic mode Rossby waves are connected through the dispersion relation:

$$c = U(k^2 + 1^2) - \beta/(k^2 + 1^2 + \lambda^{-2})$$

with $\beta = 2.3 \times 10^{-11}$ m s^{-1}, $\lambda = 115$ km, the deformation radius of the first mode, k and l as the zonal and meridional wavenumbers (2π per wavelength), respectively; and U is the background velocity (Pedlosky 1979). Estimating U to be 0.1 m s^{-1} (NECC value averaged in that area (Richardson et al. 1992), we obtain c between 6 and 10 cm s^{-1}, close to our 9 cm s^{-1} value. Following Jochum and Malanotte-Rizzoli (2003), these Rossby waves are advected eastward by the NECC until 35°W and then dissipate. Once the NECC slows or even reverses in boreal spring (Garzoli and Katz 1983; Arnault 1987; Richardson et al. 1992), the waves become westward. They reflect at the Brazilian coast, creating anticyclones. These anticyclones intensify as they propagate northwestward along the Brazilian coast because of potential vorticity conservation and become NBC rings. Thus, the LF signal we obtain, standing between 35° and 55°W with a maximum activity in October (Figs. 6b, 7b), corresponds to the retroflecting NBC Rossby waves (first mode). They can be followed until 35°W, where they vanish. They are distinct from the "equatorial" TIW peaking in August (Figs. 6c, 7c). The HF component evolution (Figs. 6a, 7a) describes the wave reflection along the Brazilian coast and the eddy formation that results, peaking now in March. Following LeBlond and Mysak (1978), an incident Rossby wave with a wavelength between 700 and 900 km will reflect with a wavelength between 400 and 500 km, and a group velocity northwestward along the Brazilian coast. This is close to our results with an incident zonal wavelength of ~700–1000 km (Fig. 6b) and the reflected one of ~500–600 km (Fig. 6a). To our knowledge, it is the first time that such a sequence is evidenced using satellite data.

Following this scenario, we assume that along the South American coast, the HF components of the SLAs are better indicators of the NBC rings than the LF ones. We combined the two first C-EOFs obtained on the HF component of the SLAs to reconstruct the "NBC ring" signal at 9°N, 53°W, which was the location of one of the North Brazil Current Ring experiments discussed, for instance, by Johns et al. (2003). Figures 9a,b give the mean number of rings obtained per trimester and then per year after this reconstruction. The HF signal presented a dominant period in March; the ring activity is dominant during the first two trimesters, as expected.

Nearly four rings can be identified during the first semester of a mean year. However, there is a large interannual variability, as the number of rings per year varies from two (in 1994 and 2008) to seven (in 2005 and 2006, for instance). Johns et al. (2003) mentioned eight to nine rings crossing this mooring between November 1998 and June 2000. We obtain the same number in our HF SLA component at that location. These rings are in phase with those numbered 1–4 and then 9–11 in Table 2 of Johns et al. (2003). The major discrepancy is due to the absence of the ring number 7 in October–November 1999 in our HF SLAs. But we have a strong signal in the

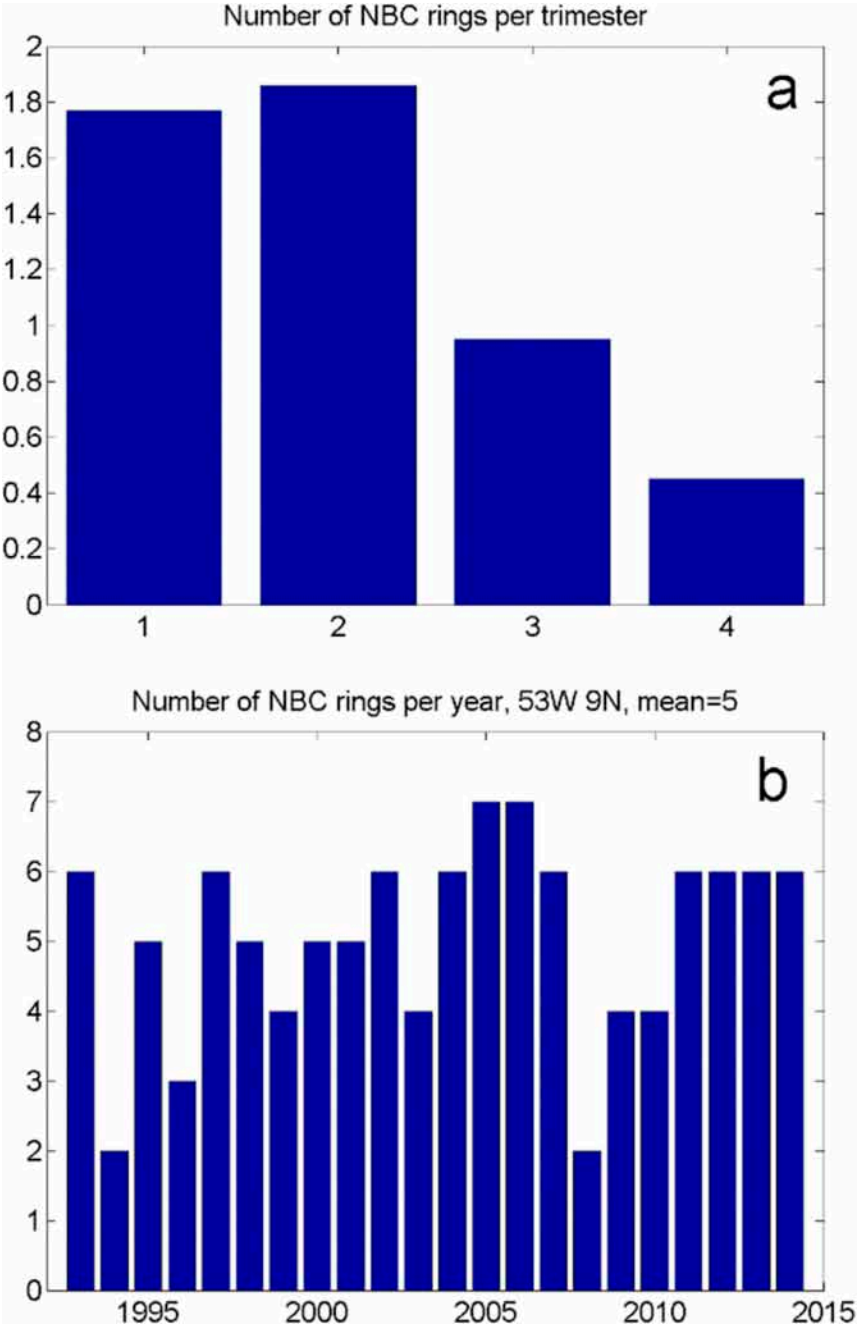

FIG. 9. (a) Average number of HF rings per trimester observed from our computations at 9°N, 53°W. (b) Number of HF rings per year observed from our computations at 9°N, 53°W.

LF component at that time (not shown). Thus, from our results, Johns et al.'s (2003) ring number 7 is mostly due to a wave meander of the NBC retroflection into the NECC than an NBC ring.

Once the different phases of the ring generation have been established, another interesting question arises about their vanishing. Previous studies do not reach the same conclusions on the subject. Fratantoni et al. (1995) mentioned that both observed and modeled NBC rings move northwestward along the coast to the islands in the southeastern region of the Caribbean, where they disintegrate, while Carton and Chao (1999) using a finer-resolution model link the eddies in the Caribbean with eddies formed outside as does Richardson (2005) from

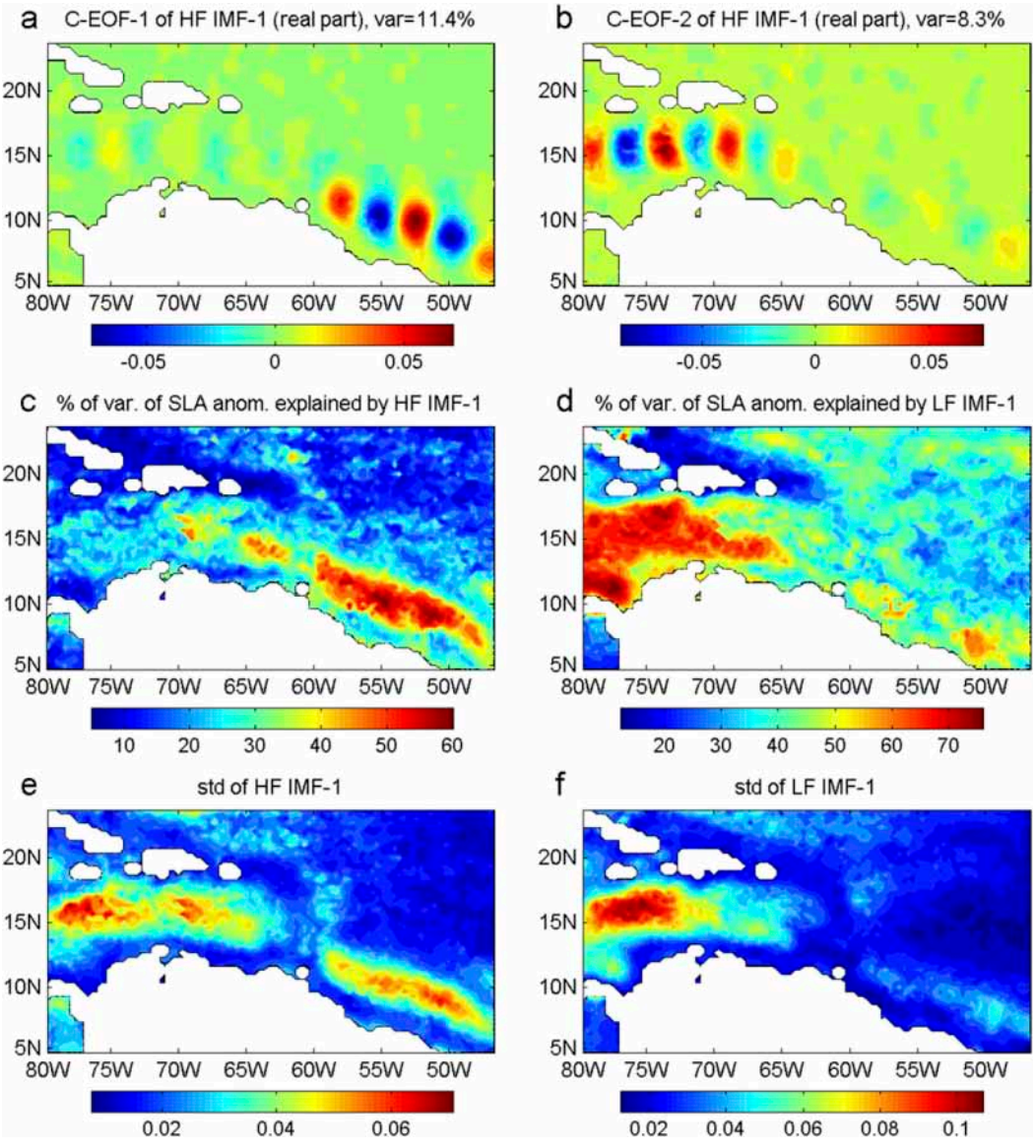

FIG. 10. (a) Real part of the first C-EOF of the SLA HF IMF-1 components between 5° and 30°N, 80° and 45°W. (b) As in (a), but for the second C-EOF. (c) Percentage of the SLA variance explained by the HF IMF-1. (d) As in (c), but for the LF IMF-1 components. (e) Std dev of the HF IMF-1 components. (f) As in (e), but for the LF IMF-1 components.

surface drifters. Goni and Johns (2003) mapped the trajectories of the rings they captured from November 1992 to December 2001 from altimetry, first moving northwestward, then once reaching 58°W usually northward, passing east of Barbados. Pauluhn and Chao (1999) found their ''altimetric'' eddies to propagate northwestward with their amplitudes, decreasing as they approach the Lesser Antilles island chain but increasing again once they enter the Caribbean Sea. Jouanno et al. (2008) find in their 1/15° resolution model that the merging and interacting between eddies is a ubiquitous process that contributes to increasing the size of eddies and that most of the Caribbean mesoscale variability originates in the eastern Caribbean basin and is not due to local processes as hypothesized before (Nystuen and Andrade 1993). We extend part of our computations northwestward from the retroflection area. Figures 10a,b display the two first C-EOFs (11.4% and 8.3%, respectively, of the explained variance) of the HF SLA. Figure 8a shows from 45° to 60°W the typical propagating eddies already observed in Fig. 6a. The period of the PC-1 is 5.8 weeks, equal again to the eddy period presented in Fig. 7a. West of 60°W, there are no more structures contrary to what is revealed by the second C-EOF, which presents structures only west

of ~65°W (Fig. 10b). The period of the corresponding PC-2 is 6.9 weeks, but the spectrum of its envelope does not show any clear seasonality contrary to those of the PC-1. It reveals energy peaks of about the same amplitude at longer periods (27, 57, and 114 weeks; not shown). Indeed, if the percentage of SLA variance explained by the HF component reaches more than 50% east of 60°W (confirming Fig. 4d), then it weakens to ~30% west of it (Fig. 10c). On the contrary, the percentage of variance caused by the LF components is more than 70% only west of 60°W (Fig. 10d). Figure 10e displays the standard deviation of the HF SLAs. There is clearly a gap between the eastern part and the western part of the area. Figure 10f gives the same picture but for the LF components and shows that the energy is concentrated in the Caribbean Sea. Thus, strictly speaking of the NBC rings discussed previously, it is clear that they ''vanish'' west of 60°W, where structures with different time and space characteristics do exist. We do not observe any important propagation of eddies northward passing east of the Barbados as suggested by Goni and Johns (2003) but a slight tendency exists (Fig. 10e). As remarked by Jochumsen et al. (2010), the complicated topography of the Lesser Antilles island arc, which separates the Atlantic Ocean from the Caribbean Sea, prohibits the undisturbed northwestward propagation of NBC rings. The way the NBC rings and the Caribbean eddies interact is however beyond the scope of this paper.

Finally, to examine the NBC ring role in the interhemispheric exchange, we need some information about the vertical structures of these rings, which is unreachable from our satellite data only. Didden and Schott (1993) assumed that each altimetric eddy they found from *Geosat* was 400 km in diameter and 350 m in thickness. The volume transport associated with the along-coast translation of one eddy per year was thus ~1.4 Sv (1 Sv $\equiv 10^6\,m^3\,s^{-1}$). Richardson et al. (1994) estimated a one-ring transport from their floats to be ~0.9 Sv, where their eddy diameter was 250 km at the surface and 140 km at 900 m. Johns et al. (1990) assumed that each eddy they found was 400 km in diameter and 200 m thick, giving a transport of ~0.8 Sv. From SeaWiFS observations and in situ tracer measurements, Fratantoni and Glickson (2002) estimated that a reasonable upper bound on the effective annualized transport of a single NBC ring is approximately 1.0 ± 0.4 Sv. Taking this latter approximation into account, a mean transport of 5 Sv yr^{-1}, mostly during the first semester, comes from our analysis, which is not negligible compared to the northward flow of the thermohaline circulation cell estimation of ~13 Sv (Schmitz and Richardson 1991; Schmitz and McCartney 1993). But, as stated in Fig. 9b and the previous paragraph: first, this estimation is highly variable from year to year; second, all the rings shown in Fig. 6b do not propagate northward and some vanish before that.

b. *TIW region*

The second area of propagating structures is located north of the equator, between 10° and 50°W (Fig. 6c). These waves show a strong seasonal cycle with maximum amplitude around August (Fig. 7c). Their length scale is ~1000 km, their period is 5.2 weeks, and their mean propagation speed is 32 km day^{-1} or 38 cm s^{-1}. These features are characteristic of the TIWs. Qiao and Weisberg (1995) present a summary of TIW observations in the Atlantic and Pacific Oceans. The reported estimates generally show westward propagation in summer and fall with period, zonal wavelength, and phase speed centered about 20–40 days, 600–1000 km, and 30–50 cm s^{-1}, respectively. The characteristics of the waves we show are in perfect agreement with these values. Thus, we can conclude that the signals presented in Figs. 6c, 7c are those of TIWs. Their period is ~36 days, and the region where they appear (north of 3°N) refers to unstable Rossby waves rather than Yanai waves (Lyman et al. 2007; Bunge et al. 2007; Han et al. 2008; Lee et al. 2012; Yin et al. 2014). We cannot conclude from our data about the generation processes (barotropic/baroclinic instabilities) of the TIW that we show, as we have no means to get the depth information. However, our results are in agreement with previous studies of these waves along 5°N from satellites (Chelton et al. 2000; Hashizume et al. 2001; Athié and Marin 2008; Foltz et al. 2004; Caltabiano et al. 2005; Lee et al. 2012, 2014). Furthermore, they add in answering a pending point: Lee et al. (2014) questioned whether the variability in the northwestern Atlantic is associated with TIWs in the traditional sense. Our method points out clearly that it has to be considered as a different phenomenon with different characteristics. In the western basin, we identify HF/small-scale structures together with LF/large-scale phenomena. These latter present characteristics that resemble equatorial TIW, but our results show that they have to be distinguished from the equatorial TIW and are due to different physical processes even if correlations can exist from time to time. Question about the existence of TIWs south of the equator is also relevant. Anomalies can be identified from our study along 5°S, west of 10°W, with wavelengths (~1000 km) comparable to the ones observed along 5°N, periods of ~4.4 weeks, and a westward propagation of ~30 cm s^{-1} (not shown). But they are of a much weaker amplitude than the northern ones.

7. Conclusions

In conclusion, the EMD-based method we have developed to identify propagating features in the tropical Atlantic Ocean gives very promising results when applied to altimetry data. The results we obtain are in good agreement with previous analyses on NECC retroflection and rings propagation, and TIWs. The advantage of this method, compared to other ones, is first to perfectly identify each of these mechanisms separately. Then to provide some information on frequency modulations, wavelengths, and other characteristics that are unreachable from other techniques. For instance, the frequency modulation we revealed in the northwestern tropical Atlantic region helps us to clarify the dynamics involved in this region and to explain some apparent disagreements between previous studies. Thanks to that property, our next step will be to investigate the modulations of the wave characteristics from an interannual point of view in order to assess the climatic impacts of these phenomena on the tropical Atlantic Ocean and neighboring countries.

Acknowledgments. The EMD program used here is available online (http://perso.ens-lyon.fr/patrick.flandrin/emd.html). This study was funded by the Centre National d'Etudes Spatiales (CNES) and the Institut de Recherche pour le Développement (IRD). SSALTO/DUACS altimeter products were produced by SSALTO/DUACS and distributed by AVISO, with support from CNES (http://www.aviso.oceanobs.com/duacs/). J. L. Mélice and S. Arnault are supported by IRD.

REFERENCES

Arnault, S., 1987: Tropical Atlantic geostrophic currents and ship drifts. *J. Geophys. Res.*, **92**, 5076–5088, doi:10.1029/JC092iC05p05076.

——, and R. E. Cheney, 1994: Tropical Atlantic sea level variability from Geosat (1985-1989). *J. Geophys. Res.*, **99**, 18 207–18 223, doi:10.1029/94JC01301.

——, Y. Ménard, and M. C. Roucquet, 1989: Variability of the tropical Atlantic in 1986–1987 as observed by GEOSAT and *in situ* data. *Adv. Space Res.*, **9**, 383–386, doi:10.1016/0273-1177(89)90189-0.

Athié, G., and F. Marin, 2008: Cross-equatorial structure and temporal modulation of intraseasonal variability at the surface of the Tropical Atlantic Ocean. *J. Geophys. Res.*, **113**, C08020, doi:10.1029/2007JC004332.

Autret, G., F. Rémy, and S. Rogues, 2013: Multiscale analysis of Antarctic surface temperature series by empirical mode decomposition. *J. Atmos. Oceanic Technol.*, **30**, 649–654, doi:10.1175/JTECH-D-11-00050.1.

Breaker, L. C., and A. Ruzmaikin, 2011: The 154-year record of sea level at San Francisco: Extracting the long-term trend, recent changes, and other tidbits. *Climate Dyn.*, **36**, 545–559, doi:10.1007/s00382-010-0865-4.

Bunge, L., C. Provost, and A. Kartavtseff, 2007: Variability in horizontal current velocities in the central and eastern equatorial Atlantic in 2002. *J. Geophys. Res.*, **112**, C02014, doi:10.1029/2006JC003704.

Caltabiano, A. C. V., I. S. Robinson, and L. P. Pezzi, 2005: Multi-year satellite observations of instability waves in the Tropical Atlantic Ocean. *Ocean Sci.*, **1**, 97–112, doi:10.5194/os-1-97-2005.

Candela, J., R. C. Beardsley, and R. Limeburner, 1992: Separation of tidal and subtidal currents in ship-mounted acoustic Doppler current profiler observations. *J. Geophys. Res.*, **97**, 769–788, doi:10.1029/91JC02569.

Carton, J. A., 1989: Estimates of sea level in the tropical Atlantic Ocean using Geosat altimetry. *J. Geophys. Res.*, **94**, 8029–8039, doi:10.1029/JC094iC06p08029.

——, and Y. Chao, 1999: Caribbean Sea eddies inferred from TOPEX/POSEIDON altimetry and a 1/6° Atlantic Ocean model simulation. *J. Geophys. Res.*, **104**, 7743–7752, doi:10.1029/1998JC900081.

Castelão, G. P., and W. E. Johns, 2011: Sea surface structure of North Brazil Current rings derived from shipboard and moored acoustic Doppler current profiler observations. *J. Geophys. Res.*, **116**, C01010, doi:10.1029/2010JC006575.

Chambers, D. P., 2015: Evaluation of the empirical mode decomposition for quantifying multi-decadal variations and acceleration in sea level records. *Nonlinear Processes Geophys.*, **22**, 157–166, doi:10.5194/npg-22-157-2015.

Chelton, D. B., F. J. Wentz, C. L. Gentemann, R. A. de Szoeke, and M. G. Schlax, 2000: Satellite microwave SST observations of transequatorial tropical instability waves. *Geophys. Res. Lett.*, **27**, 1239–1242, doi:10.1029/1999GL011047.

Chen, X., Y. Feng, and N. E. Huang, 2014: Global sea level trend during 1993–2012. *Global Planet. Change*, **112**, 26–32, doi:10.1016/j.gloplacha.2013.11.001.

Cohen, L., P. Loughlin, and D. Vakman, 1999: On an ambiguity in the definition of the amplitude and phase of a signal. *Signal Process.*, **79**, 301–307, doi:10.1016/S0165-1684(99)00103-6.

Delprat, N., B. Escuidé, P. Guillemain, R. Kronland-Martinet, P. Tchamitchian, and B. Torrésani, 1992: Asymptotic wavelet and Gabor analysis: Extraction of instantaneous frequencies. *IEEE Trans. Inf. Theory*, **38**, 644–664, doi:10.1109/18.119728.

Didden, N., and F. Schott, 1993: Eddies in the North Brazil Current retroflection region observed by Geosat altimetry. *J. Geophys. Res.*, **98**, 20 121–20 131, doi:10.1029/93JC01184.

Düing, W., and Coauthor, 1975: Meanders and long waves in the equatorial Atlantic. *Nature*, **257**, 280–284, doi:10.1038/257280a0.

Ezer, T., and W. B. Corlett, 2012: Is sea level rise accelerating in the Chesapeake Bay? A demonstration of a novel new approach for analyzing sea level data. *Geophys. Res. Lett.*, **39**, L19605, doi:10.1029/2012GL053435.

——, L. P. Atkinson, W. B. Corlett, and J. L. Blanco, 2013: Gulf Stream's induced sea level rise and variability along the U.S. mid-Atlantic coast. *J. Geophys. Res. Oceans*, **118**, 685–697, doi:10.1002/jgrc.20091.

Foltz, G. R., J. A. Carton, and E. P. Chassignet, 2004: Tropical instability vortices in the Atlantic Ocean. *J. Geophys. Res.*, **109**, C03029, doi:10.1029/2003JC001942.

Fratantoni, D. M., and D. A. Glickson, 2002: North Brazil Current ring generation and evolution observed with SeaWiFS. *J. Phys. Oceanogr.*, **32**, 1058–1074, doi:10.1175/1520-0485(2002)032<1058:NBCRGA>2.0.CO;2.

——, and P. L. Richardson, 2006: The evolution and demise of North Brazil Current rings. *J. Phys. Oceanogr.*, **36**, 1241–1264, doi:10.1175/JPO2907.1.

——, W. E. Johns, and T. L. Townsend, 1995: Rings of the North Brazil Current: Their structure and behavior inferred from

observations and a numerical simulation. *J. Geophys. Res.*, **100**, 10 633–10 654, doi:10.1029/95JC00925.

——, ——, ——, and H. E. Hurlburt, 2000: Low-latitude circulation and mass transport pathways in a model of the tropical Atlantic Ocean. *J. Phys. Oceanogr.*, **30**, 1944–1966, doi:10.1175/1520-0485(2000)030<1944:LLCAMT>2.0.CO;2.

Garzoli, S. L., and E. J. Katz, 1983: The forced annual reversal of the Atlantic North Equatorial Countercurrent. *J. Phys. Oceanogr.*, **13**, 2082–2090, doi:10.1175/1520-0485(1983)013<2082:TFAROT>2.0.CO;2.

——, A. Field, and Q. Yao, 2003: North Brazil current rings and the variability in the latitude of retroflection. *Interhemispheric Water Exchange in the Atlantic Ocean*, G. J. Goni and P. Malanotte-Rizzoli, Eds., Elsevier Oceanography Series, Vol. 68, Elsevier Science, 357–373.

Goni, G. J., and W. E. Johns, 2001: A census of North Brazil Current Rings observed from TOPEX/POSEIDON altimetry: 1992–1998. *Geophys. Res. Lett.*, **28**, 1–4, doi:10.1029/2000GL011717.

——, and ——, 2003: Synoptic study of warm rings in the North Brazil current retroflection region using satellite altimetry. *Interhemispheric Water Exchange in the Atlantic Ocean*, G. J. Goni and P. Malanotte-Rizzoli, Eds., Elsevier Oceanography Series, Vol. 68, Elsevier Science, 335–356.

Grodsky, S., J. Carton, C. Provost, J. Servain, J. Lorenzzetti, and M. McPhaden, 2005: Tropical instability waves at 0°N, 23°W in the Atlantic: A case study using Pilot Research Moored Array in the Tropical Atlantic (PIRATA) mooring data. *J. Geophys. Res.*, **110**, C08010, doi:10.1029/2005JC002941.

Halliwell, G. R., Jr., R. H. Weisberg, and D. A. Mayer, 2003: A synthetic float analysis of upper-limb meridional overturning circulation interior ocean pathways in the tropical/subtropical Atlantic. *Interhemispheric Water Exchange in the Atlantic Ocean*, G. J. Goni and P. Malanotte-Rizzoli, Eds., Elsevier Oceanography Series, Vol. 68, Elsevier Science, 93–136.

Han, W., P. J. Webster, J. Lin, W. T. Liu, R. Fu, D. Yuan, and A. Hu, 2008: Dynamics of intraseasonal sea level and thermocline variability in the equatorial Atlantic during 2002–03. *J. Phys. Oceanogr.*, **38**, 945–967, doi:10.1175/2008JPO3854.1.

Hashizume, H., S. P. Xie, T. W. Liu, and K. Takeuchi, 2001: Local and remote atmospheric response to tropical instability waves: A global view from space. *J. Geophys. Res.*, **106**, 10 173–10 185, doi:10.1029/2000JD900684.

Huang, N. E., and Coauthors, 1998: The empirical mode decomposition and the Hilbert spectrum for nonlinear and non-stationary time series analysis. *Proc. Roy. Soc. London*, **454A**, 903–995, doi:10.1098/rspa.1998.0193.

Jochum, M., and P. Malanotte-Rizzoli, 2003: On the generation of North Brazil Current rings. *J. Mar. Res.*, **61**, 147–173, doi:10.1357/002224003322005050.

——, ——, and A. Busalacchi, 2004: Tropical instability waves in the Atlantic Ocean. *Ocean Modell.*, **7**, 145–163, doi:10.1016/S1463-5003(03)00042-8.

Jochumsen, K., M. Rhein, S. Hüttl-Kabus, and C. W. Böning, 2010: On the propagation and decay of North Brazil Current rings. *J. Geophys. Res.*, **115**, C10004, doi:10.1029/2009JC006042.

Johns, W. E., T. N. Lee, F. Schott, R. Zantopp, and R. Evans, 1990: The North Brazil Current retroflection: Seasonal structure and eddy variability. *J. Geophys. Res.*, **95**, 22 103–22 120, doi:10.1029/JC095iC12p22103.

——, R. J. Zantopp, and G. J. Goni, 2003: Cross-gyre transport by North Brazil Current rings. *Interhemispheric Water Exchange in the Atlantic Ocean*, G. J. Goni and P. Malanotte-Rizzoli, Eds., Elsevier Oceanography Series, Vol. 68, Elsevier Science, 411–441.

Jouanno, J., J. Scheinbaum, B. Barnier, J. M. Molines, L. Debreu, and F. Lemarié, 2008: The mesoscale variability in the Caribbean Sea. Part I: Simulations and characteristics with an embedded model. *Ocean Modell.*, **23**, 82–101, doi:10.1016/j.ocemod.2008.04.002.

Kelly, B., S. Meyers, and J. O'Brien, 1995: On a generating mechanism for Yanai waves and the 25-day oscillation. *J. Geophys. Res.*, **100**, 10 589–10 612, doi:10.1029/94JC02911.

LeBlond, P. H., and L. A. Mysak, 1978: *Waves in the Ocean.* Elsevier, 602 pp.

Lee, H. S., 2013: Estimation of extreme sea levels along the Bangladesh coast due to storm surge and sea level rise using EEMD and EVA. *J. Geophys. Res. Oceans*, **118**, 4273–4285, doi:10.1002/jgrc.20310.

Lee, T., G. Lagerloef, M. M. Gierach, H.-Y. Kao, S. Yueh, and K. Dohan, 2012: Aquarius reveals salinity structure of tropical instability waves. *Geophys. Res. Lett.*, **39**, L12610, doi:10.1029/2012GL052232.

——, ——, H.-Y. Kao, M. J. McPhaden, J. Willis, and M. M. Gierach, 2014: The influence of salinity on tropical Atlantic instability waves. *J. Geophys. Res. Oceans*, **119**, 8375–8394, doi:10.1002/2014JC010100.

Legeckis, R., 1977: Long waves in the eastern equatorial Pacific Ocean: A view from a geostationary satellite. *Science*, **197**, 1179–1181, doi:10.1126/science.197.4309.1179.

Lyman, J., G. Johnson, and W. Kessler, 2007: Distinct 17- and 33-day tropical instability waves in subsurface observations. *J. Phys. Oceanogr.*, **37**, 855–872, doi:10.1175/JPO3023.1.

Mayer, D. A., and R. H. Weisberg, 1993: A description of COADS surface meteorological fields and the implied Sverdrup transports for the Atlantic Ocean from 30°S to 60°N. *J. Phys. Oceanogr.*, **23**, 2201–2221, doi:10.1175/1520-0485(1993)023<2201:ADOCSM>2.0.CO;2.

McClean, J. L., and J. M. Klinck, 1995: Description and dynamics of 50-day oscillations in the western tropical region of the CME model. *J. Phys. Oceanogr.*, **25**, 2498–2517, doi:10.1175/1520-0485(1995)025<2498:DAVAOD>2.0.CO;2.

McCreary, J., and Z. Yu, 1992: Equatorial dynamics in a 2 1/2-layer model. *Prog. Oceanogr.*, **29**, 61–132, doi:10.1016/0079-6611(92)90003-I.

Menkes, C., and Coauthors, 2002: A whirling ecosystem in the equatorial Atlantic. *Geophys. Res. Lett.*, **29**, 1553, doi:10.1029/2001GL014576.

Merle, J., M. Fieux, and P. Hisard, 1980: Annual signal and interannual anomalies of SST in the eastern equatorial Atlantic Ocean. *Oceanography and Surface Layer Meteorology in the B/C Scale*, G. Siedler and J. D. Woods, Eds., Pergamon Press, 77–101, doi:10.1016/B978-1-4832-8366-1.50023-6.

Navarra, A., and V. Simoncini, 2010: *A Guide to Empirical Orthogonal Functions for Climate Data Analysis.* Springer, 158 pp., doi:10.1007/978-90-481-3702-2_1.

Nof, D., and T. Pichevin, 1996: The retroflection paradox. *J. Phys. Oceanogr.*, **26**, 2344–2358, doi:10.1175/1520-0485(1996)026<2344:TRP>2.0.CO;2.

Nystuen, J. A., and C. A. Andrade, 1993: Tracking mesoscale ocean features in the Caribbean Sea using Geosat altimetry. *J. Geophys. Res.*, **98**, 8389–8394, doi:10.1029/93JC00125.

Pauluhn, A., and Y. Chao, 1999: Tracking eddies in the subtropical north-western Atlantic Ocean. *Phys. Chem. Earth*, **24A**, 415–421, doi:10.1016/S1464-1895(99)00052-6.

Pedlosky, J., 1979: *Geophysical Fluid Dynamics*. Springer, 707 pp.

Philander, S. G. H., 1978: Instability of zonal equatorial currents, 2. *J. Geophys. Res.*, **83**, 3679–3682, doi:10.1029/JC083iC07p03679.

——, W. J. Hurlin, and R. C. Pacanowski, 1986: Properties of long equatorial waves in models of the seasonal cycle in the tropical Atlantic and Pacific Oceans. *J. Geophys. Res.*, **91**, 14 207–14 211, doi:10.1029/JC091iC12p14207.

Picinbono, B., 1997: On the instantaneous amplitude and phase of signals. *IEEE Trans. Signal Process.*, **45**, 552–560, doi:10.1109/78.558469.

Poularikas, A. D., 1996: *The Transforms and Applications Handbook*. CRC and IEEE Press, 1336 pp.

Proehl, J. A., 1996: Linear stability of equatorial zonal flows. *J. Phys. Oceanogr.*, **26**, 601–621, doi:10.1175/1520-0485(1996)026<0601:LSOEZF>2.0.CO;2.

Pujol, M.-I., Y. Faugère, G. Taburet, S. Dupuy, C. Pelloquin, M. Ablain, and N. Picot, 2016: DUACS DT2014: The new multi-mission altimeter data set reprocessed over 20 years. *Ocean Sci.*, **12**, 1067–1090, doi:10.5194/os-12-1067-2016.

Qiao, L., and R. H. Weisberg, 1995: Tropical instability wave kinematics: Observations from the Tropical Instability Wave Experiment. *J. Geophys. Res.*, **100**, 8677–8693, doi:10.1029/95JC00305.

Richardson, P. L., 2005: Caribbean Current and eddies as observed by surface drifters. *Deep-Sea Res. II*, **52**, 429–463, doi:10.1016/j.dsr2.2004.11.001.

——, S. Arnault, S. Garzoli, and J. Bruce, 1992: Annual cycle of the Atlantic North Equatorial Countercurrent. *Deep-Sea Res.*, **39A**, 997–1014, doi:10.1016/0198-0149(92)90036-S.

——, G. E. Hufford, R. Limeburner, and W. S. Brown, 1994: North Brazil Current retroflection eddies. *J. Geophys. Res.*, **99**, 5081–5093, doi:10.1029/93JC03486.

Rilling, G., P. Flandrin, and P. Gonçalvès, 2003: On empirical mode decomposition and its algorithms. *Proc. IEEE-EURASIP Workshop on Nonlinear Signal and Image Processing (NSIP-30)*, Grado, Italy, IEEE/EURASIP, 5 pp., https://hal.inria.fr/inria-00570628.

——, ——, P. Goncalves, and J. M. Lilly, 2007: Bivariate empirical mode decomposition. *IEEE Signal Process. Lett.*, **14**, 936–939, doi:10.1109/LSP.2007.904710.

Salisbury, J. I., and M. Wimbush, 2002: Using modern time series analysis techniques to predict ENSO events from SOI time series. *Nonlinear Processes Geophys.*, **9**, 341–354, doi:10.5194/npg-9-341-2002.

Schmitz, W. J., Jr., and P. L. Richardson, 1991: On the sources of the Florida Current. *Deep-Sea Res.*, **38A** (Suppl.), S379–S409, doi:10.1016/S0198-0149(12)80018-5.

——, and M. S. McCartney, 1993: On the North Atlantic circulation. *Rev. Geophys.*, **31**, 29–49, doi:10.1029/92RG02583.

Vakman, D., 1996: On the analytical signal, the Teager-Kaiser energy algorithm, and other methods for defining amplitude and frequency. *IEEE Trans. Signal Process.*, **44**, 791–797, doi:10.1109/78.492532.

von Schuckmann, K., P. Brandt, and C. Eden, 2008: Generation of tropical instability waves in the Atlantic Ocean. *J. Geophys. Res.*, **113**, C08034, doi:10.1029/2007JC004712.

Weisberg, R. H., 1980: Equatorial waves during GATE and their relation to the mean zonal circulation. *Oceanography and Surface Layer Meteorology in the B/C Scale*, G. Siedler and J. D. Woods, Eds., Pergamon Press, 179–198, doi:10.1016/B978-1-4832-8366-1.50028-5.

——, and T. J. Weingartner, 1988: Instability waves in the equatorial Atlantic Ocean. *J. Phys. Oceanogr.*, **18**, 1641–1657, doi:10.1175/1520-0485(1988)018<1641:IWITEA>2.0.CO;2.

Yin, X., J. Boutin, G. Reverdin, T. Lee, N. Martin, and S. Arnault, 2014: SMOS Sea Surface Salinity signatures of tropical instability waves. *J. Geophys. Res. Oceans*, **119**, 7811–7826, doi:10.1002/2014JC009960.